Oxygen Evolution

DOI: 10.1002/anie.201403946

Graphitic Carbon Nitride Nanosheet–Carbon Nanotube Three-Dimensional Porous Composites as High-Performance Oxygen Evolution Electrocatalysts**

*Tian Yi Ma, Sheng Dai, Mietek Jaroniec, and Shi Zhang Qiao**

Abstract: *A new class of highly efficient oxygen evolution catalysts has been synthesized through the self-assembly of graphitic carbon nitride nanosheets and carbon nanotubes, driven by π–π stacking and electrostatic interactions. Remarkably, the catalysts exhibit higher catalytic oxygen evolution activity and stronger durability than Ir-based noble-metal catalysts and display the best performance among the reported nonmetal catalysts. This good result is attributed to the high nitrogen content and the efficient mass and charge transfer in the porous three-dimensional nanostructure.*

The design of highly active and stable catalysts for the oxygen evolution reaction (OER) is urgently needed because the OER is the efficiency-limiting process for many important electrochemical energy conversion devices, such as metal–air batteries and fuel cells,[1] and the most efficient catalysts for the sluggish OER are still noble metals, that is, Ir- and Ru-based materials.[2] To replace expensive Ir and Ru, numerous efforts have been undertaken toward using transition-metal alternatives (Co, Fe, Mn, etc.),[3] in which metal species are considered to be the active sites. However, the complicated fabrication procedure and low conductivity largely limit the applications of metal oxides, which in most cases underperform noble-metal catalysts. In contrast to the metal-based catalysts, nonmetal OER catalysts consisting of less expensive earth-abundant elements (C, H, O, N) that act also as the active-site-forming elements are rarely reported. Only a few reports have been devoted to N-active materials, including organic *N*(5)-ethylflavinium ions[4] and N-doped graphene–carbon nanotube composites,[5] but the catalytic activity is still unsatisfactory. A recent breakthrough was achieved by synthesizing N-doped graphitic carbon (N/C) materials, which afforded a $10\,mA\,cm^{-2}$ current density at 1.61 V versus the reversible hydrogen electrode (RHE),[6] a value approaching that of IrO_2/C. The pyridinic and quaternary N atoms were proven to be the active sites for the OER, similarly to those in the reverse oxygen reduction reaction (ORR) catalyzed by N-doped carbon materials;[7] however, in this case, Ni species were added in the preparation process to graphitize the N/C catalysts. Despite some drawbacks, these efforts inspired us to seek for N-rich and highly conductive (graphitic) carbon materials that are able to efficiently catalyze the OER.

Carbon doped with N can greatly improve the stability of the resultant catalysts, due to enhanced π bonding in the framework, and promote their electron donor–acceptor properties, which enhances their catalytic activity for specific electrochemical reactions.[7] Among various precursors, graphitic carbon nitride ($g\text{-}C_3N_4$) is especially promising for introducing N into carbon materials, due to its high N content, low cost, and easily tailorable structure;[8] however, scarce efforts have been made to employ $g\text{-}C_3N_4$ as the active material for the electrocatalytic OER. Optimal use of $g\text{-}C_3N_4$ for electrochemical applications requires the improvement of its poor conductivity. Generally, two types of method have been applied, that is, physical mixing of $g\text{-}C_3N_4$ with conductive carbon materials[9] and in situ immobilization of $g\text{-}C_3N_4$ onto carbon supports.[7b,d,10] The poor contact and inhomogeneity between physically mixed $g\text{-}C_3N_4$ aggregates and carbon are the major disadvantages of the former method, whereas, for the latter route, the high-temperature polymerization ($\geq 500\,°C$) of the monomers (for example, dicyandiamide and melamine) to produce $g\text{-}C_3N_4$ inside the carbon matrix may undesirably lead to substantial reduction of the N content. Thus, a better fabrication strategy that assures a strong interaction between $g\text{-}C_3N_4$ and the carbon support at relatively low temperatures is highly desirable. Recently, two-dimensional (2D) $g\text{-}C_3N_4$ nanosheets ($g\text{-}C_3N_4$ NSs) were synthesized by destacking the layered bulk $g\text{-}C_3N_4$ through thermal oxidation etching[11] and liquid exfoliation.[12] Although these two strategies still suffer from extremely low yield and a long sonication time (10–16 h), respectively, the opening of the interlayer space in this layered material enlarges its surface area, which is promising for improving its interaction with other substances (for example, carbon) and reactants and, consequently, for enhancing its electrical and chemical properties relative to those of the bulk counterpart.

Herein, we report the facile low-temperature self-assembly of $g\text{-}C_3N_4$ NSs and carbon nanotubes (CNTs) to obtain strongly coupled composite OER catalysts (denoted as $g\text{-}C_3N_4$ NS–CNT). The utilization of $g\text{-}C_3N_4$ NSs as the precursor instead of bulk $g\text{-}C_3N_4$ facilitates the robust assembly to form a three-dimensional (3D) interconnected network, which possesses a well-developed porous structure with a large surface area ($149\,m^2\,g^{-1}$) and high N content

[*] Dr. T. Y. Ma, Prof. S. Dai, Prof. S. Z. Qiao
School of Chemical Engineering, The University of Adelaide
Adelaide, SA 5005 (Australia)
E-mail: s.qiao@adelaide.edu.au
Prof. M. Jaroniec
Department of Chemistry and Biochemistry, Kent State University
Kent, OH 44240 (USA)

[**] This work is financially supported by the Australian Research Council (ARC) through the Discovery Project programs (DP140104062 and DP130104459).

Supporting information for this article is available on the WWW under http://dx.doi.org/10.1002/anie.201403946.

(23.7 wt %). These electrocatalysts display better activity and stronger durability than the nanosized IrO_2 catalyst supported on CNTs (denoted as IrO_2–CNT; for synthesis details, see the Supporting Information).

2D g-C_3N_4 NSs were first prepared by sonication/exfoliation of protonated g-C_3N_4 (Scheme 1). The protonation was

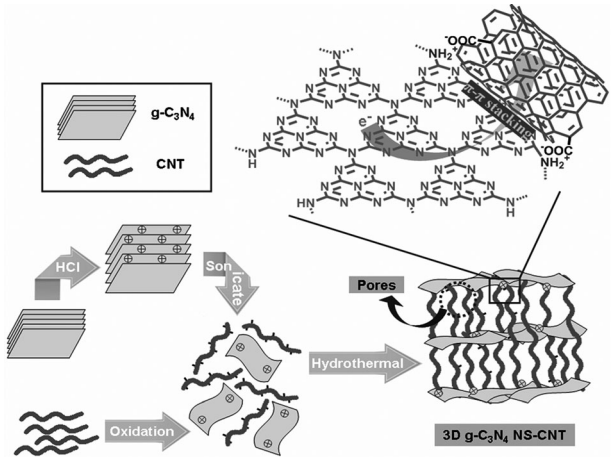

Scheme 1. Fabrication of the 3D g-C_3N_4 NS–CNT porous composite.

conducted by using concentrated hydrochloric acid, which not only efficiently reduced the subsequent exfoliation time to approximately 2 h (compared with 10–16 h without protonation[12]) due to disruption of the interplanar and inplanar cohesion in the bulk g-C_3N_4 (for example, van der Waals forces and hydrogen bonding),[13] but also afforded g-C_3N_4 NSs with a positively charged surface (zeta potential of +25.6 mV versus −37.3 mV for pristine g-C_3N_4). The spontaneous assembly between the mildly oxidized CNTs (zeta potential of −19.3 mV) with abundant oxygen-containing functional groups (for example, COO^-) and the positively charged g-C_3N_4 NSs was then achieved through a hydrothermal process driven by electrostatic and π–π stacking interactions to form a 3D composite with numerous pores (see the details in the Supporting Information).

The as-synthesized 2D g-C_3N_4 NSs exhibit a thin layered structure (see the scanning electron microscopy (SEM) images in Figure S1 a,b in the Supporting Information) with a negligible amount of bulk domains, which indicates the high efficiency of the exfoliation process used. The nearly transparent layers reveal the very thin thickness (see the transmission electron microscopy (TEM) images in Figure S1 c,d) and are consistent with the atomic force microscopy (AFM) observations, which show a thickness of approximately 3.2 nm, equal to 9–10 CN atomic monolayers (Figure 1 a). Unlike the loosely dispersed g-C_3N_4 NSs, the g-C_3N_4 NS–CNT composite material is assembled by bridging CNTs (Figure 1 b), into a 3D porous network composed of thin nanolayers and closely grafted CNTs within the interlayer space, as shown in the magnified SEM image (Figure 1 c). The uniform dispersion of N and C elements in g-C_3N_4 NS–CNT (see the EDS elemental mapping image in the inset of Figure 1 b) verifies a homogeneous distribution of closely interconnected

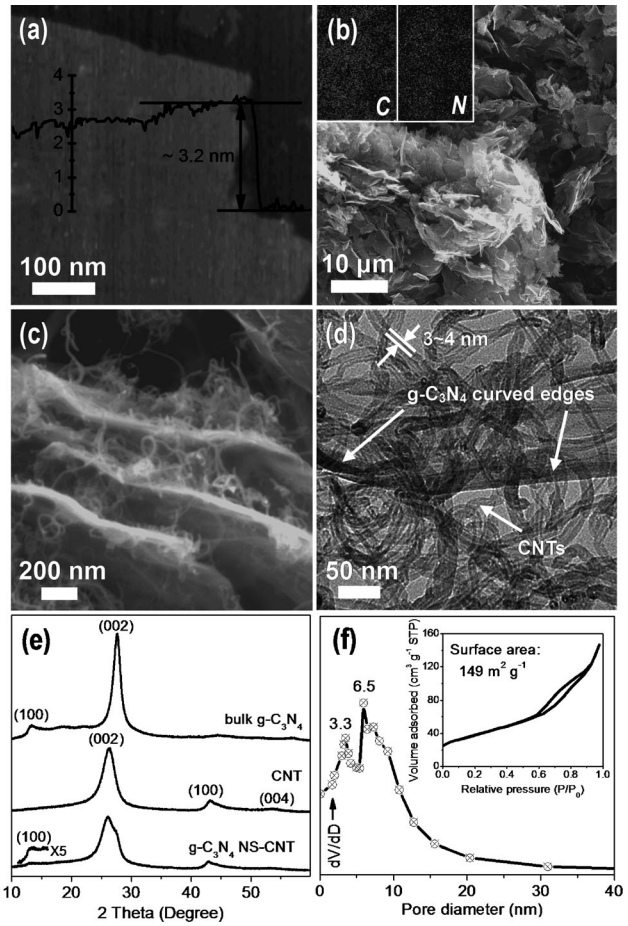

Figure 1. a) AFM image of g-C_3N_4 NSs. b,c) SEM and d) TEM images of g-C_3N_4 NS–CNT. Inset in (b): Energy dispersive X-ray spectroscopy (EDS) elemental mapping. e) X-ray diffraction (XRD) patterns of g-C_3N_4 NS–CNT, the CNTs, and g-C_3N_4. f) The pore-size distribution curve. Inset: The N_2 adsorption isotherm recorded for g-C_3N_4 NS–CNT.

g-C_3N_4 NSs and CNTs (see the TEM image in Figure 1 d). Thus, the microscopy images show a well-connected porous network composed of CNTs coupled with g-C_3N_4 NSs.

It is noteworthy that the characteristic structural features of g-C_3N_4 and CNTs are well preserved in the 3D g-C_3N_4 NS–CNT composite. The presence of g-C_3N_4 domains is verified by two signals present on the XRD pattern (Figure 1 e), namely the strong shoulder peak at 2θ of 27.4° ($d = 0.326$ nm), which originates from the (002) interlayer diffraction of a CN graphitic-like structure, and the low-angle diffraction peak at 2θ of 13.3° ($d = 0.663$ nm), which is derived from inplanar repeated tri-s-triazine units. Notably, the intensity of these two peaks is sharply reduced relative to that in the bulk g-C_3N_4 due to the few-layer structure and smaller planar size of the NSs after exfoliation.[11,12] The N_2 adsorption isotherm measured for g-C_3N_4 NS–CNT resembles type IV with an H3-type hysteresis loop (Figure 1 f), which confirms the presence of interconnected mesopores. Correspondingly, two peaks at 3.3 and 6.5 nm are observed on the pore-size distribution curve, which are probably attributable to the inner cavity diameter of the CNTs and the pores formed in the assembled 3D matrix, respectively. In addition, g-C_3N_4 NS–CNT exhibits

a large surface area of 149 $m^2 g^{-1}$, which is consistent with the highly porous structure visible on the microscopy images.

Strong coupling between the g-C_3N_4 NSs and CNTs in the assembled 3D g-C_3N_4 NS–CNT was firstly confirmed by X-ray photoelectron spectroscopy (XPS), in which both the N 1s and C 1s spectra of g-C_3N_4 NS–CNT (Figure 2) show distinct profiles relative to those of g-C_3N_4 (Figure S2). Specifically, the best deconvolution of the N 1s spectrum was achieved by

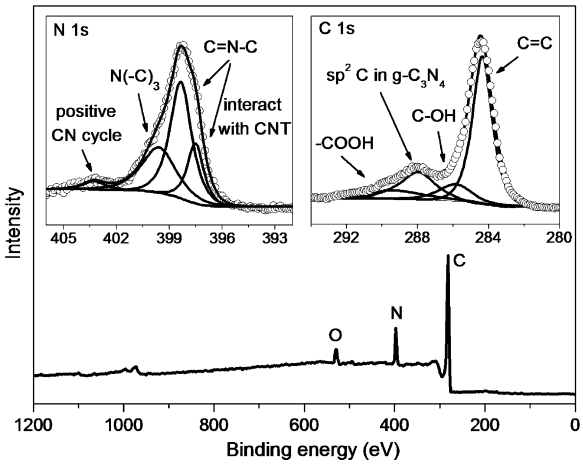

Figure 2. XPS survey and high-resolution spectra of N 1s and C 1s core levels in g-C_3N_4 NS–CNT.

the assumption of four species. The peak at 399.8 eV can be attributed to the bridging N atoms in N(−C)$_3$ or N atoms bonded with H atoms. The dominant peak at 398.3 eV corresponds to the sp^2-bonded N atoms in triazine rings (C–N=C); this peak splits to form an obvious new shoulder peak at 397.6 eV, which is caused by the strong interaction between the CNTs and the N atoms in the g-C_3N_4 NSs.[14] Another peak at 403.3 eV is due to the protonation of g-C_3N_4 NSs, which renders CN heterocycles and cyano groups positively charged.[15] The C 1s spectrum of g-C_3N_4 NS–CNT can be deconvoluted into four species, that is, the sp^2-bonded C atoms in the g-C_3N_4 NSs (288.0 eV)[11,12] and the C=C (284.6 eV), C–OH (285.7 eV), and COOH (289.1 eV) species in the CNTs.[16] The XPS survey spectrum shows that g-C_3N_4 NS–CNT contains C, N, and O atoms with a high N content of 23.7 wt%, which is consistent with the elemental analysis result (Table S1). Moreover, as seen from the Fourier transform infrared (FTIR) spectra (Figure S3), the characteristic bands for the CN heterocycle stretching vibration in g-C_3N_4 NS–CNT show blueshifts relative to those of g-C_3N_4, for example, 1390→1371 cm^{-1} and 1538→1522 cm^{-1}; this effect is also due to the strong interaction between the CNTs and g-C_3N_4 NSs. A new band centered at approximately 1730 cm^{-1} is ascribed to the presence of carboxyl groups on the mildly oxidized CNTs.

The strong coupling between the CNTs and g-C_3N_4 NSs proven by the microscopy images and the XPS and FTIR spectroscopy results is related to the robust self-assembly during the hydrothermal aging process. The driving force for the self-assembly of the CNTs and g-C_3N_4 NSs can be attributed to two aspects: the π–π stacking interaction between conjugated tri-s-triazine motifs in the g-C_3N_4 NSs and graphene fragments in the CNTs, and the electrostatic interaction between COO^- groups on the CNTs (289.1 eV in C 1s XPS; 1730 cm^{-1} in FTIR spectroscopy) and the positively charged g-C_3N_4 NSs (zeta potential of + 25.6 mV; 403.3 eV in N 1s XPS).

The remarkable 3D porous structure composed of strongly coupled CNTs and g-C_3N_4 NSs reveals the great potential of g-C_3N_4 NS–CNT for the electrocatalytic OER. A slow scan rate (5 mV s^{-1}) was applied during the OER test on a rotating disk electrode (RDE) in alkaline solutions (0.1 M KOH) to minimize the capacitive current. In the linear sweep voltammograms (LSVs; Figure 3a and Figure S4, S5),

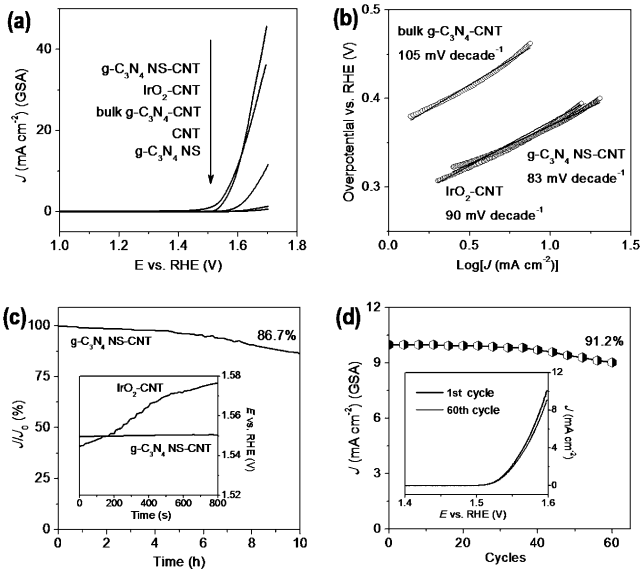

Figure 3. a) LSVs and b) Tafel plots for g-C_3N_4 NS–CNT, IrO_2–CNT, bulk g-C_3N_4–CNT, purified oxidized CNTs, and g-C_3N_4 NSs on a RDE (1500 rpm) in an O_2-saturated 0.1 M KOH solution (scan rate: 5 mV s^{-1}). The calculation of the OER current density was based on the geometric surface area (GSA).[2,3] c) Chronoamperometric response at a constant potential of 1.54 V. Inset: Chronopotentiometric response of g-C_3N_4 NS–CNT as compared with that of IrO_2-CNT at a constant current density of 3.0 mA cm^{-2}. d) A curve of the current density of g-C_3N_4 NS–CNT at 1.60 V versus scan cycles. Inset: LSVs of g-C_3N_4 NS–CNT before and after 60 scan cycles (scan rate: 5 mV s^{-1}).

the purified oxidized CNTs and g-C_3N_4 NSs show negligible OER response, which indicates that the trace metal residues in the CNTs (see the details in the Supporting Information) hardly contribute to the catalytic OER activity. The anodic current recorded on g-C_3N_4 NS–CNT renders a sharp onset potential at approximately 1.53 V, which shows clearly that the coupling of two components can significantly improve the catalytic activity. IrO_2–CNT affords a slightly lower onset potential (approximately 1.51 V), but its OER current density drops below that of g-C_3N_4 NS–CNT at potentials higher than 1.62 V, at which point g-C_3N_4 NS–CNT features a better performance.

The operating potentials (versus RHE) to deliver a 10 mA cm^{-2} current density were compared; this is the

value expected for a 10% efficient solar water-splitting device.[17] The 3D g-C_3N_4 NS–CNT material generates a current density of 10 mA cm^{-2} at 1.60 V, similar to the value for IrO_2–CNT (1.59 V) and comparable to those of the state-of-the-art noble-metal catalysts, for example, IrO_2/C (1.60 V, 0.1 M KOH),[6] colloidal IrO_2 nanoparticles (1.60 V, 0.5 M H_2SO_4),[18] and $Ru_{0.2}Ir_{0.8}O_2$ (1.61 V, 0.5 M H_2SO_4),[19] and the transition-metal catalysts, for example, $Mn_3O_4/CoSe_2$ hybrids (1.68 V, 0.1 M KOH)[20] and Co_3O_4/N-graphene (1.63 V, 1 M KOH).[3d] The activity of g-C_3N_4 NS–CNT is also higher than that of the previously reported *N*(5)-ethylflavinium ions[4] and N-doped graphene–CNT composites (> 1.65 V, 0.1 M KOH).[5]

The catalytic kinetics for the OER was examined by Tafel plots (Figure 3b). The lower Tafel slope value for g-C_3N_4 NS–CNT (83 mV decade^{-1}) indicates its more favorable kinetics relative to that of IrO_2–CNT (90 mV decade^{-1}). This result agrees with the higher catalytic current density of g-C_3N_4 NS–CNT than that of IrO_2–CNT in the high potential region (> 1.62 V; Figure 3a and Figure S6), which suggests better catalytic activity for g-C_3N_4 NS–CNT.

The chronoamperometric response demonstrates the high stability of g-C_3N_4 NS–CNT and shows a slight anodic current attenuation of 13.3% within 10 h (Figure 3c and Figure S7). This insignificant activity decrease may be caused by a small mass loss of the catalyst due to its partial peeling by a large amount of the evolved oxygen. Also, in the chronopotentiometric response, g-C_3N_4 NS–CNT displays a nearly constant operating potential at 1.55 V to deliver a 3.0 mA cm^{-2} current density (inset of Figure 3c), whereas the potential of IrO_2–CNT shows an increase of approximately 32 mV within 800 s, which reveals that g-C_3N_4 NS–CNT has higher stability than IrO_2–CNT. Furthermore, 91.2% of the original catalytic current can be retained after 60 scan cycles at a scan rate of 5 mV s^{-1} (Figure 3d). A stable catalytic performance in high-concentration alkaline solutions is critical for realistic applications.[17] In 1 M KOH, the high activity of g-C_3N_4 NS–CNT is well preserved with a sharp onset potential of 1.47 V, and the chronopotentiometric response shows its operating potential to be stable at approximately 1.48 V to deliver a 2.0 mA cm^{-2} current density (Figure S8), which corroborates the effective operation of g-C_3N_4 NS–CNT in concentrated electrolytes.

To gain insight into the reaction mechanism, the rotating ring-disk electrode (RRDE) technique was employed with a Pt ring electrode potential of 1.50 V to detect the peroxide species formed at the g-C_3N_4 NS–CNT catalyst surface during the OER. A very low ring current (μA scale) was recorded (Figure 4a), which is three orders of magnitude lower than that of the disk current (mA scale) and suggests almost no formation of hydrogen peroxide. This result indicates that g-C_3N_4 NS–CNT favors a desirable four-electron water-oxidation pathway. To ensure that the observed oxidation current is from oxygen evolution, a RRDE was applied in N_2-saturated 0.1 M KOH solution. With the disk current at 200 μA, O_2 molecules generated from the catalyst on the disk sweep across the surrounding Pt ring held at an ORR potential of 0.40 V and are rapidly reduced (Figure 4b). Thus, a ring current of approximately 40 μA (200 μA × 0.2; RRDE collecting efficiency = 0.2) was detected, which suggests that the

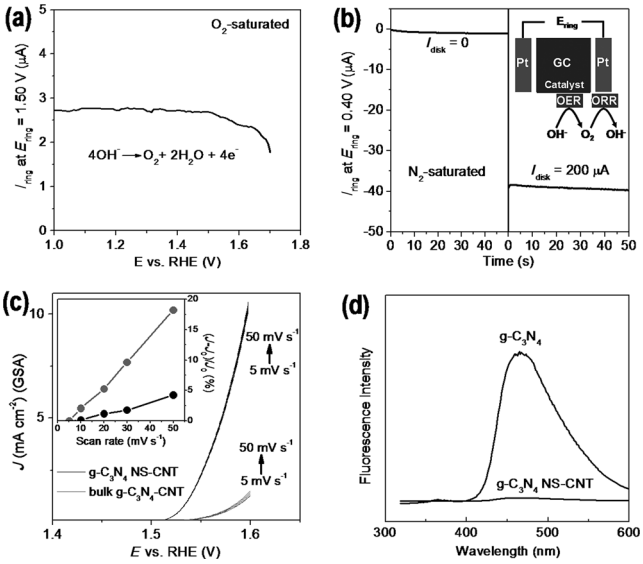

Figure 4. a) The ring current of g-C_3N_4 NS–CNT on a RRDE (1500 rpm) in O_2-saturated 0.1 M KOH solution (ring potential: 1.50 V). b) The ring current of g-C_3N_4 NS–CNT on a RRDE (1500 rpm) in N_2-saturated 0.1 M KOH solution (ring potential: 0.40 V). c) LSVs of g-C_3N_4 NS–CNT and bulk g-C_3N_4–CNT at different scan rates. Inset: The corresponding data replotted as the current density (at 1.60 V) increased percentage versus scan rates. d) Fluorescence emission spectra of g-C_3N_4 NS–CNT and g-C_3N_4.

observed oxidation current can be fully related to the OER. Accordingly, the Faradaic efficiency of g-C_3N_4 NS–CNT was calculated to be approximately 99.2%.

The outstanding OER activity of g-C_3N_4 NS–CNT originates from its high N content (high concentration of active sites), unique porous architecture (fast mass transport), and strong coupling between the g-C_3N_4 NSs and CNTs (good electron conductivity). Firstly, g-C_3N_4 NS–CNT features a high N content of 23.7 wt%, which surpasses that of the most N-doped carbon catalysts reported,[7a,b,d,10] because the new low-temperature synthesis affords strong coupling between the g-C_3N_4 NSs and CNTs. The extensively present electron-accepting pyridinic and tertiary N species can impart a relatively high positive charge density on the neighboring sp^2-bonded C atoms.[7a] In accordance with the OER pathway in alkaline solutions ($4OH^- \rightarrow O_2 + 2H_2O + 4e^-$), the positive carbon atoms can facilitate adsorption of OH^- ions, promote the electron transfer between the catalyst surface and reaction intermediates (for example, O^{2-} ions), and assure an easy recombination of two adsorbed oxygen atoms for O_2 evolution.[21]

Secondly, to illustrate the importance of the porous 3D structure, bulk g-C_3N_4–CNT was prepared for the purpose of comparison by coupling CNTs with bulk g-C_3N_4 instead of g-C_3N_4 NSs (see the details in the Supporting Information), which resulted in a nonporous structure with a low surface area of 32 m^2 g^{-1} (Figure S9). Bulk g-C_3N_4–CNT shows low OER activity and unfavorable kinetics compared with those of g-C_3N_4 NS–CNT (Figure 3). Its current density is more susceptible to the scan rate and showed a variation of 18.7% (compared with 4.8% for g-C_3N_4 NS–CNT) upon an increase

in the scan rate from 5 to 50 $mV s^{-1}$ (Figure 4c), due to the restricted mass transfer in the nonporous solid. These facts demonstrate the importance of the highly porous 3D architecture in g-C_3N_4 NS–CNT, which favors the easy infiltration of electrolytes, the efficient transfer of reactants (that is, OH^- ions), and the fast emission of products (that is, O_2).

Thirdly, the poor electron transfer in g-C_3N_4 is the primary barrier for its use in electrocatalytic applications,[7b,c,d,8] which is conquered herein by strong coupling of highly conductive CNTs with semiconducting g-C_3N_4 (as evidenced by microscopy images and XPS and FTIR spectroscopy). The smooth transfer of the generated catalytic current through the π–π stacking between the g-C_3N_4 NSs and CNTs is proven by fluorescence emission spectra (Figure 4d). Relative to the high fluorescence intensity of g-C_3N_4, the fluorescence is completely quenched in g-C_3N_4 NS–CNT, which indicates that the photogenerated electrons on the g-C_3N_4 NSs can be easily transferred to the CNTs. In contrast, the inferior interaction and electron transport between bulk g-C_3N_4 and the CNTs in the bulk g-C_3N_4–CNT catalyst is another reason for its low OER activity besides the limited mass transfer. Due to the aforementioned three advantages, a series of 3D composites with different g-C_3N_4 NS/CNT ratios was synthesized with high catalytic activity for the OER (Figure S10, S11 and Table S1).

In summary, 3D g-C_3N_4 NS–CNT porous composites are reported to exhibit the highest activity among nonmetal OER catalysts and better performance with more favorable kinetics and stronger durability than noble-metal catalysts. Their outstanding activity can be attributed to the large amount of active sites, related to the high N concentration, and the improved charge and mass transport abilities due to the 3D interconnected porous framework. Further efforts will be made toward fabrication of self-supported electrodes to increase their long-term stability and toward replacement of the CNTs with other low-price carbon supports to reduce the cost.

Received: April 2, 2014
Published online: June 2, 2014

Keywords: carbon · electrocatalysis · nanostructures · oxygen evolution · porous structure

[1] a) T. Ogasawara, A. Débart, M. Holzapfel, P. Novák, P. G. Bruce, *J. Am. Chem. Soc.* **2006**, *128*, 1390 – 1393; b) N. S. Lewis, *Science* **2007**, *315*, 798 – 801; c) R. F. Service, *Science* **2009**, *324*, 1257 – 1259.

[2] a) M. G. Walter, E. L. Warren, J. R. McKone, S. W. Boettcher, Q. Mi, E. A. Santori, N. S. Lewis, *Chem. Rev.* **2010**, *110*, 6446 – 6473; b) Y. Lee, J. Suntivich, K. J. May, E. E. Perry, Y. Shao-Horn, *J. Phys. Chem. Lett.* **2012**, *3*, 399 – 404.

[3] a) W. C. Ellis, N. D. McDaniel, S. Bernhard, T. J. Collins, *J. Am. Chem. Soc.* **2010**, *132*, 10990 – 10991; b) Q. Yin, J. M. Tan, C. Besson, Y. V. Geletii, D. G. Musaev, A. E. Kuznetsov, Z. Luo, K. I. Hardcastle, C. L. Hill, *Science* **2010**, *328*, 342 – 345; c) J. Suntivich, K. J. May, H. A. Gasteiger, J. B. Goodenough, Y. Shao-Horn, *Science* **2011**, *334*, 1383 – 1385; d) Y. Liang, Y. G. Li, H. L. Wang, J. G. Zhou, J. Wang, T. Regier, H. J. Dai, *Nat. Mater.* **2011**, *10*, 780 – 786.

[4] E. Mirzakulova, R. Khatmullin, J. Walpita, T. Corrigan, N. M. Vargas-Barbosa, S. Vyas, S. Oottikkal, S. F. Manzer, C. M. Hadad, K. D. Glusac, *Nat. Chem.* **2012**, *4*, 794 – 801.

[5] a) S. Chen, J. J. Duan, M. Jaroniec, S. Z. Qiao, *Adv. Mater.* **2014**, *26*, 2925 – 2930; b) H. W. Park, D. U. Lee, Y. Liu, J. Wu, L. F. Nazar, Z. Chen, *J. Electrochem. Soc.* **2013**, *160*, A2244 – A2250.

[6] Y. Zhao, R. Nakamura, K. Kamiya, S. Nakanishi, K. Hashimoto, *Nat. Commun.* **2013**, *4*, 2390.

[7] a) K. Gong, F. Du, Z. Xia, M. Durstock, L. Dai, *Science* **2009**, *323*, 760 – 764; b) Y. Zheng, Y. Jiao, J. Chen, J. Liu, J. Liang, A. Du, W. Zhang, Z. Zhu, S. C. Smith, M. Jaroniec, G. Q. Lu, S. Z. Qiao, *J. Am. Chem. Soc.* **2011**, *133*, 20116 – 20119; c) Y. Zheng, Y. Jiao, Y. Jin, M. Jaroniec, S. Z. Qiao, *Small* **2012**, *8*, 3550 – 3566; d) J. Liang, Y. Zheng, J. Chen, J. Liu, D. Hulicova-Jurcakova, M. Jaroniec, S. Z. Qiao, *Angew. Chem.* **2012**, *124*, 3958 – 3962; *Angew. Chem. Int. Ed.* **2012**, *51*, 3892 – 3896.

[8] a) A. Thomas, A. Fischer, F. Goettmann, M. Antonietti, J. O. Müller, R. Schlögl, J. M. Carlsson, *J. Mater. Chem.* **2008**, *18*, 4893 – 4908; b) Y. Wang, X. Wang, M. Antonietti, *Angew. Chem.* **2012**, *124*, 70 – 92; *Angew. Chem. Int. Ed.* **2012**, *51*, 68 – 89.

[9] S. M. Lyth, Y. Nabae, S. Moriya, S. Kuroki, M. Kakimoto, J. Ozaki, S. Miyata, *J. Phys. Chem. C* **2009**, *113*, 20148 – 20151.

[10] a) S. M. Lyth, Y. Nabae, N. M. Islam, S. Kuroki, M. Kakimoto, S. Miyata, *J. Electroanal. Chem.* **2011**, *158*, B194 – B201; b) S. Yang, X. Feng, X. Wang, K. Müllen, *Angew. Chem.* **2011**, *123*, 5451 – 5455; *Angew. Chem. Int. Ed.* **2011**, *50*, 5339 – 5343; c) Y. Sun, C. Li, Y. Xu, H. Bai, Z. Yao, G. Shi, *Chem. Commun.* **2010**, *46*, 4740 – 4742.

[11] P. Niu, L. Zhang, G. Liu, H. M. Cheng, *Adv. Funct. Mater.* **2012**, *22*, 4763 – 4770.

[12] a) X. Zhang, X. Xie, H. Wang, J. Zhang, B. Pan, Y. Xie, *J. Am. Chem. Soc.* **2013**, *135*, 18 – 21; b) J. Tian, Q. Liu, A. M. Asiri, A. O. Al-Youbi, X. Sun, *Anal. Chem.* **2013**, *85*, 5595 – 5599; c) S. Yang, Y. Gong, J. Zhang, L. Zhan, L. Ma, Z. Fang, R. Vajtai, X. Wang, P. M. Ajayan, *Adv. Mater.* **2013**, *25*, 2452 – 2456.

[13] a) B. V. Lotsch, M. Doblinger, J. Sehnert, L. Seyfarth, J. Senker, O. Oeckler, W. Schnick, *Chem. Eur. J.* **2007**, *13*, 4969 – 4980; b) J. N. Coleman, *Acc. Chem. Res.* **2013**, *46*, 14 – 22; c) T. Y. Ma, Y. H. Tang, S. Dai, S. Z. Qiao, *Small* **2014**, DOI: 10.1002/smll.201303827.

[14] Q. Liu, J. Zhang, *Langmuir* **2013**, *29*, 3821 – 3828.

[15] a) D. Foy, *J. Solid State Chem.* **2009**, *182*, 165 – 171; b) R. C. Dante, P. Martin-Ramos, A. Correa-Guimaraes, J. Martin-Gil, *Mater. Chem. Phys.* **2011**, *130*, 1094 – 1102.

[16] Y. Zheng, Y. Jiao, L. Ge, M. Jaroniec, S. Z. Qiao, *Angew. Chem.* **2013**, *125*, 3192 – 3198; *Angew. Chem. Int. Ed.* **2013**, *52*, 3110 – 3116.

[17] C. C. L. McCrory, S. Jung, J. C. Peters, T. F. Jaramillo, *J. Am. Chem. Soc.* **2013**, *135*, 16977 – 16987.

[18] W. Hu, Y. Wang, X. Hu, Y. Zhou, S. Chen, *J. Mater. Chem.* **2012**, *22*, 6010 – 6016.

[19] N. Mamaca, E. Mayousse, S. Arrii-Clacens, T. W. Napporn, K. Servat, N. Guillet, K. B. Kokoh, *Appl. Catal. B* **2012**, *111 – 112*, 376 – 380.

[20] M. R. Gao, Y. F. Xu, J. Jiang, Y. R. Zheng, S. H. Yu, *J. Am. Chem. Soc.* **2012**, *134*, 2930 – 2933.

[21] a) R. Cao, J. S. Lee, M. Liu, J. Cho, *Adv. Energy Mater.* **2012**, *2*, 816 – 829; b) H. Wang, H. Dai, *Chem. Soc. Rev.* **2013**, *42*, 3088 – 3113.

